Supplementary Information for:

Internal deformation of the subducted Nazca slab inferred from seismic anisotropy

Caroline M. Eakin[1,2*], Maureen D. Long[1], Alissa Scire[3], Susan L. Beck[3], Lara S. Wagner[4], George Zandt[3], Hernando Tavera[5]

1. Department of Geology and Geophysics, Yale University, New Haven, Connecticut, USA

2. University of Southampton, National Oceanography Centre, Southampton, UK

3. Department of Geosciences, University of Arizona, Tucson, Arizona, USA

4. Department of Terrestrial Magnetism, Carnegie Institution for Science, Washington, DC, USA

5. Instituto Geofísico del Perú, Lima, Peru

* Corresponding author

Raypath calculation

We estimate raypaths for all local *S* and source-side measurements using a 1D velocity model (iasp91[1]) with a localized crustal correction to account for the variable thickness of the Andes across our study region (see Table S1). We opt to use this velocity structure as it was the same background velocity model used for constructing the tomography[2] to which we compare our results (e.g. Figure 2). However, given that any 3D wave propagation effects are not incorporated, it is likely that we are actually underestimating the path lengths through the slab material, as the fast slab may act as a waveguide. This suggests that paths that appear to fall close to the slab based on the 1D velocity model may actually sample large portions of the slab itself. This may explain why the red non-slab splits near 72°W, 15°S in Figure 1 have similar characteristics to the nearby slab splits in blue towards the east.

Depth of the anisotropic source

The similarity of the splitting characteristics between the local *S* and the teleseismic *S* measurements for slab paths suggests that the main source of the anisotropy must lie somewhere in the depth range at which they both overlap (~200-550 km). It is therefore highly likely that the anisotropic source is in the upper mantle and/or the upper transition zone, suggesting that anisotropic wadsleyite or dense hydrous magnesium silicates (DHMS)[3] could also play a role in addition to olivine. The pattern of local *S* splitting, however, particularly the two anomalous splits (green bars, Figure 2a) with slow arrival times, contrasting fast directions, and upper mantle raypaths that fall outside the slab, are best explained by a primary source of anisotropy in the upper mantle and not in the transition zone. This is because at transition zone depths the raypaths of all the local *S* phases, including the two

anomalous measurements, have yet to diverge considerably from their common source (Figure S1), and so the Fresnel zones will still overlap.

Looking at each dataset individually, the teleseismic *S* measurements also sample the mid-mantle below 550km depth, which has been shown to possess significant anisotropy within some subduction zones[4–7]. Beneath our study region in South America, using deep (>500 km) earthquakes and raypaths that are solely confined to the slab within the transition zone, we previously found a predominance of null results (i.e. a lack of splitting) for teleseismic *S* phases[8]. This suggests that at least for the raypath geometries we are using, the deepest part of the Nazca slab in this region (at depths > 500 km) does not appear anisotropic.

The local *S* measurements presented in this study sample the uppermost mantle above 200 km depth, in addition to the depth region that we infer is the major source of anisotropy (~200-550 km). We previously analyzed shear wave splitting from local earthquakes at depths between ~50-170 km using the same stations as in the present study[9]; these measurements directly isolate the supra-slab anisotropic contribution from the overriding plate. We found the anisotropy in this layer to be incoherent (variable ϕ) and roughly an order of magnitude weaker (mean δt: 0.29 seconds) compared to splitting from the deep local *S* events (mean δt: 1.29 seconds). The dominant anisotropic signal for our deep local *S* events must therefore come from the subducted slab below 200 km, as the effect of the uppermost mantle will be small (Figure S9).

Modeling anisotropy within the subducting Nazca slab

(i) Assuming a frozen-in fossil fabric

We take the elastic constants for different olivine LPO fabrics[10], as well as a natural peridotite sample[11], and rotate the elastic tensor into the subducted slab geometry. This we do under the Bunge Euler convention[26], whereby we rotate the tensor first into the dip direction (determined by finding the gradient of the slab contours in Figure 1), and then tilt it into the correct dip. Finally we rotate the tensor in the dip plane to account for the angular difference between the dip direction versus the plate motion direction (i.e. to account for the obliquity of subduction). These rotations are performed using the Matlab Seismic Anisotropy Toolkit (MSAT) [13], and are repeated for each individual raypath in the sub-dataset of splitting measurements that sample the slab. We pick the dip, dip direction and plate motion direction values based on the location of the raypath at 300 km depth, as this appears to be the midpoint of travel through the slab for most observations. The plate motion vectors are absolute velocities based on model HS3-NUVEL1A [14]. The current day absolute plate motion and the paleo-spreading direction (derived from the gradient of seafloor age) are very similar for the Nazca plate, so we use the absolute plate motion model as a proxy for the paleo-spreading direction, for ease of calculation.

Once the elastic tensor is in the correct orientation, we consider a plane wave propagating with the associated inclination and azimuth of the raypath under question (see Figure S10), and solve the Christoffel equation to predict the orientation of the fast quasi-*S* wave (i.e. ϕ) and the strength of the anisotropy (%) using the MS_phasevels function within MSAT [13].

(ii) Searching for the best-fitting orientation of olivine LPO (A-type)

We perform the grid search using 10° increments from 0°-350° for each of the three Euler rotation angles (ϕ_1, θ, ϕ_2), where ϕ_1 is a rotation about the z axis, θ is a

rotation about the new x axis, and ϕ_2 is a second rotation about the new z axis [12,13]. For the starting model the x, y, and z axes correspond to east, north, and vertical respectively, while the *a*-axis points down-dip, the *b*-axis is aligned with the slab strike, and the *c*-axis is orthogonal to both *a* and *b* (i.e., normal to the slab surface).

We identify the best-fitting orientation as that which minimizes the mean angular misfit for all splitting measurements. We purposely omitted delay time observations from our modeling framework, as we did not find these to be helpful for constraining the models. The underlying reasons for this are several-fold; delay times estimates tend to have relatively larger associated errors, there is less variability in the observations, and most importantly there is a complete trade-off between the strength of the anisotropy and the thickness of the anisotropic material. Without knowing the precise distance travelled through the slab for each individual raypath it is difficult to make accurate predictions of the accumulated delay time. For example, every 10 km of uncertainty in the path length will propagate into a 0.1 second error into the predicted delay time. Given that we are not including 3D effects in our raypath calculations (such as a slab waveguide effect), estimating the path length through the slab for every measurement would likely lead to the introduction of unnecessary error in our modeling results. Instead, we demonstrate in Figure S6 the range of path lengths that would be required in order to reproduce the delay times in our dataset, given the anisotropic strength predicted by different models. This calculation demonstrates that we can match the observed delay times with a reasonable range of path lengths in the anisotropic models.

Our forward modeling exercise for A-type fabric identified a best-fitting rotation of $\phi_1 = 350°$, $\theta = 100°$, $\phi_2 = 350°$, which acts to apply an almost orthogonal rotation of the fast *a*-axis from the down-dip starting position to sub-parallel with the

slab strike (yellow star, Figure 3). The mean angular misfit for this best fit model is 18°, which is smaller than the standard error bars on individual splitting measurements, and a histogram of the misfit displays a skew towards 0°, as would be expected for a model that provides a good fit to the data (Figure S4).

(iii) Searching for the best-fitting orientation of wadsleyite

Unlike olivine, experimental constraints on LPO development in wadsleyite, especially under transition zone conditions, are not well established. Single crystal elastic tensors, however, are available [15–17], and these demonstrate that wadsleyite crystals are intrinsically anisotropic. We perform the same modeling process and grid search to find the best-fitting orientation of (single-crystal) wadsleyite [15] as we did for A-type olivine. The only difference is that we use the geometrical characteristics of the slab (dip angle and dip direction) in the upper transition zone (mid-point 460 km) to define the starting model. The rotation that best fits the data is $\phi_1 = 230°$, $\theta = 20°$, $\phi_2 = 140°$, with an average misfit of 15° (Figure S4). For the top 1% of models, however, the wadsleyite *a*-axes appear to cluster around 3 different potential orientations: parallel to the slab strike, parallel to the slab dip, and intermediate between the strike and dip but within the same plane parallel to the slab surface (Figure S7a).

(iv) Considering SPO mechanisms

If the intra-slab anisotropy was generated by shape preferred orientation (SPO) instead of LPO then the pattern of faulting required to explain fast directions parallel to the slab contours would suggest fault planes (or layering) with a similar dip and strike to that of the slab (Figure S7b). This is very different to the predicted

orientation of faulting that would have been generated by outer-rise bending[18] (Figure S11). Additionally this faulting does not penetrate throughout the whole slab, but to a maximum depth of 20-30km[3], and therefore only the upper part of the slab will be hydrated. Given that seismic tomography only tells us about the extent of the fast anomaly associated with the slab, we cannot constrain to what extent our raypaths are sensitive to this potentially hydrated top layer or to the bulk of the slab.

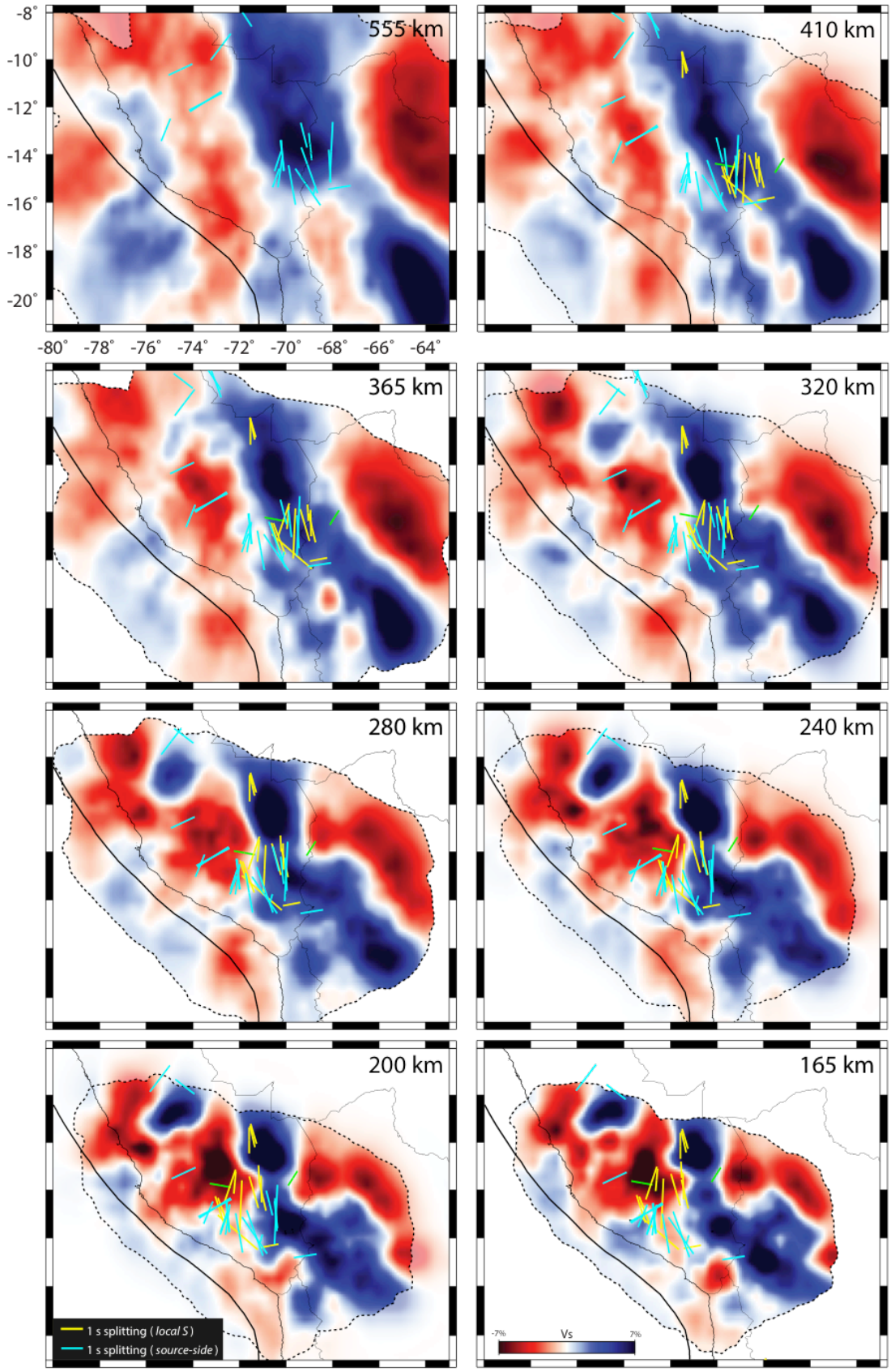

Figure S1. Shear wave splitting results overlain on *S*-wave tomography [2] at different depth slices. Splitting measurements are projected to their pierce-point location, i.e.

the location of the raypath, at each depth. Splits are color-coded yellow and turquoise for local *S* and source-side, respectively. The orientation of the bar represents ϕ, and the length is scaled by δt. For many of the measurements, often with N-S ϕ, the raypaths spend a significant portion of their journey travelling through the slab (approximately linear dark blue feature). The two local *S* splits shaded green are those which do not display a significant travel time anomaly in Figure 2b.

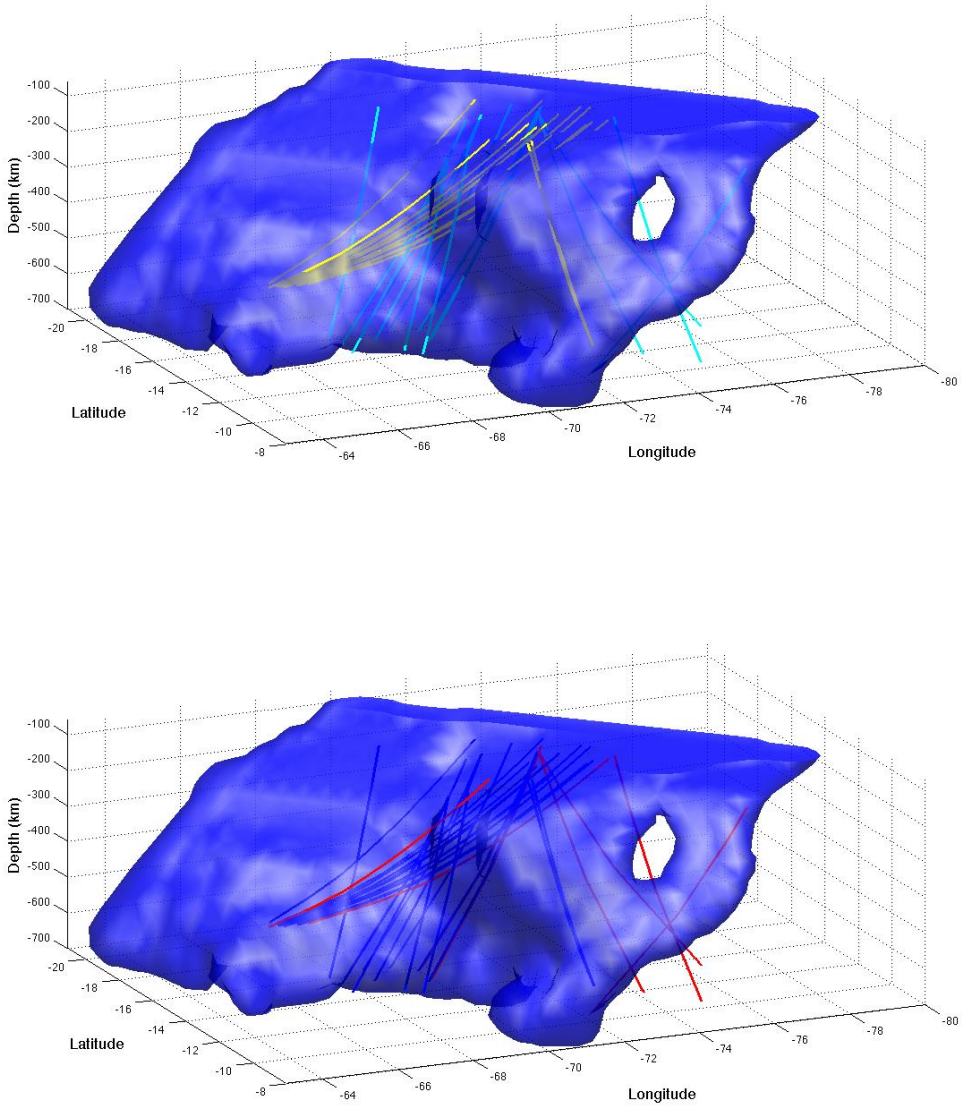

Figure S2. Freeze-frames of Movie S1 showing the slab geometry and location of raypaths. Further explanation of the images is provided in the caption for Movie S1.

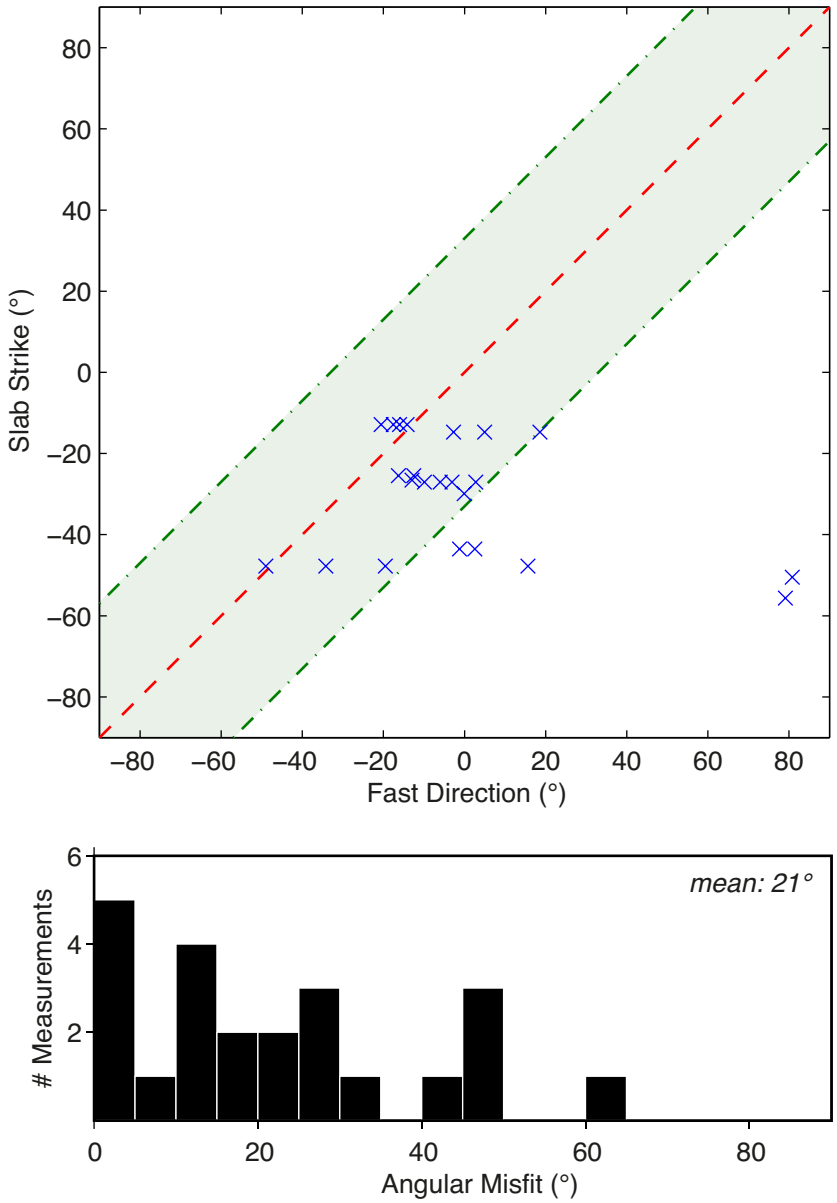

Figure S3. Plot of the fast directions of our slab splitting dataset versus the local strike of the slab at 300 km pierce-point (i.e. a graphical representation of the blue bars in Figure 1 versus the slab contours). Over 75% of the measurements (18/23) fall within 33° of the slab strike (green zone). The box below shows the same data as above but instead we plot a histogram of the angular difference between the slab strike and the fast directions, similar to Figure S4.

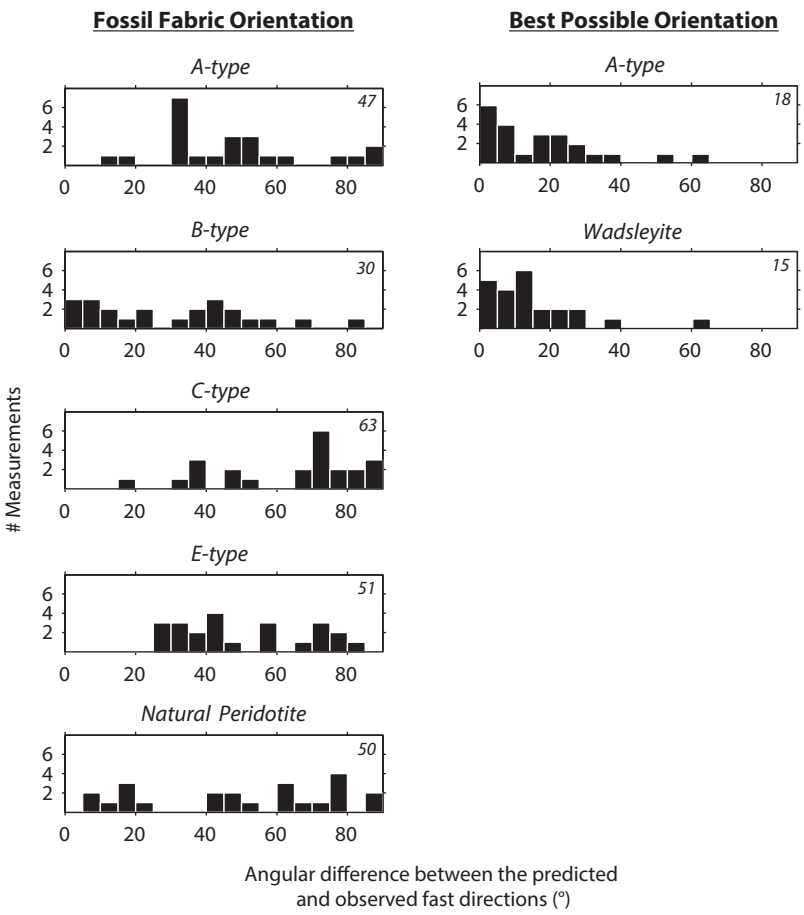

Figure S4. Histograms showing how well fossilized anisotropy within the Nazca slab can fit our slab splitting results for different olivine LPO fabrics (left column). None of the fabrics provide a particularly good fit to the dataset, for which we would expect a clustering near zero misfit. For comparison, the corresponding histograms for the best-fitting orientation of A-type olivine and single crystal wadsleyite (yellow stars in Figures 3 and S7a) are shown on the right hand column. The number in the top right hand corner of each plot is the mean misfit angle.

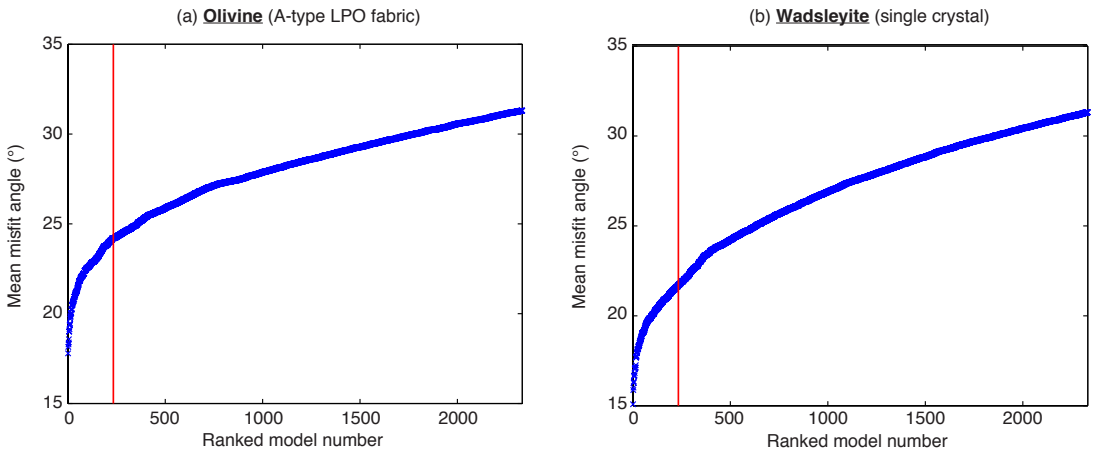

Figure S5. The mean angular misfit (difference between the predicted and observed ϕ) for the top 10% of models for (a) olivine A-type fabric, and (b) wadsleyite single crystal anisotropy. The top 1% of models, as plotted in the pole figures in Figures 3 and S7a, is marked by the red line and corresponds to a change in slope, i.e. a considerable improvement in fit. For this reason, the characteristics of the top 1% of models is discussed in the text and shown in Figure 3.

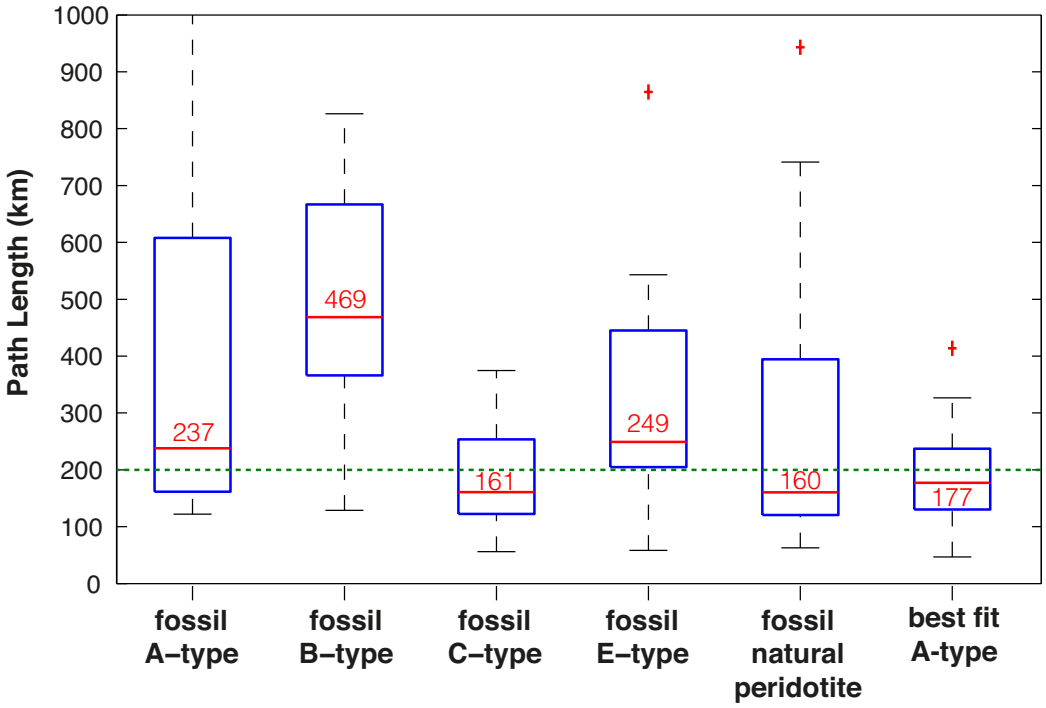

Figure S6. Boxplot distributions showing the total path length of anisotropic material that would be required to explain the range of delay times in our slab splitting dataset for different models from Figure S4. Numbers in red give the median values also shown by the red line. The blue boxes extend from the lower to upper quartiles, and the red crosses represent outliers. The green dashed line at 200 km compares the distance that we estimate that our raypaths have travelled through the slab. Overall the best-fit and fossil C-type models provide the most reasonable range of predicted path lengths.

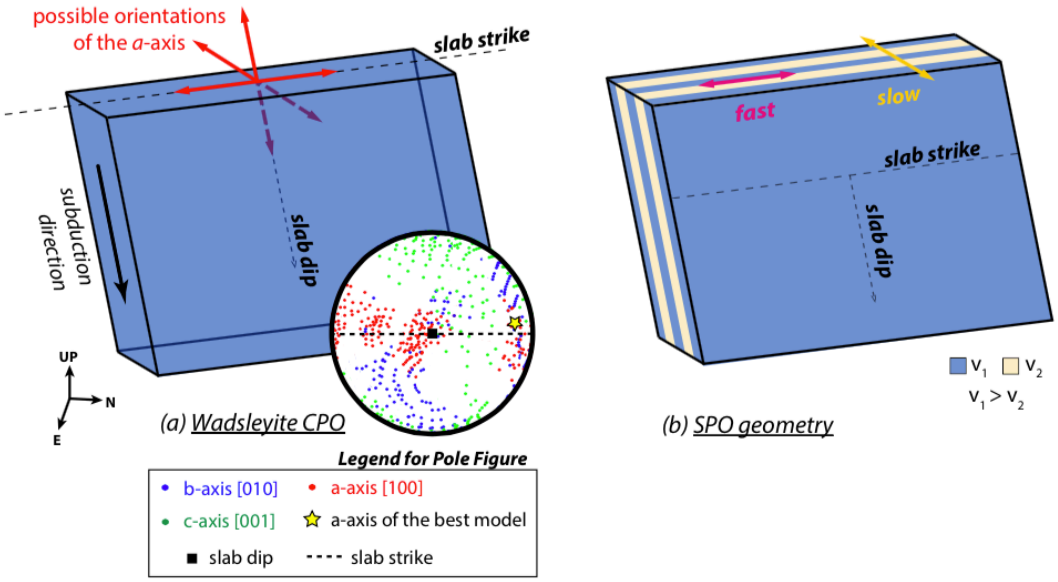

Figure S7. Illustration of alternative mechanisms that could reproduce our slab splitting results. (a) Pole figure (upper hemisphere plotted, looking from above) show the crystal preferred orientation (CPO) of the main crystal axes (*a*, *b*, and *c*) that would be required by single-crystal wadsleyite in the transition zone, for the top 1% of models. For wadsleyite the *b*- and *c*-axes are randomly oriented, but the *a*-axes tend to cluster around certain orientations. These favorable *a*-axis orientations are illustrated on the blue cartoon slab. (b) Geometry of layering for a shape preferred orientation (SPO) mechanism.

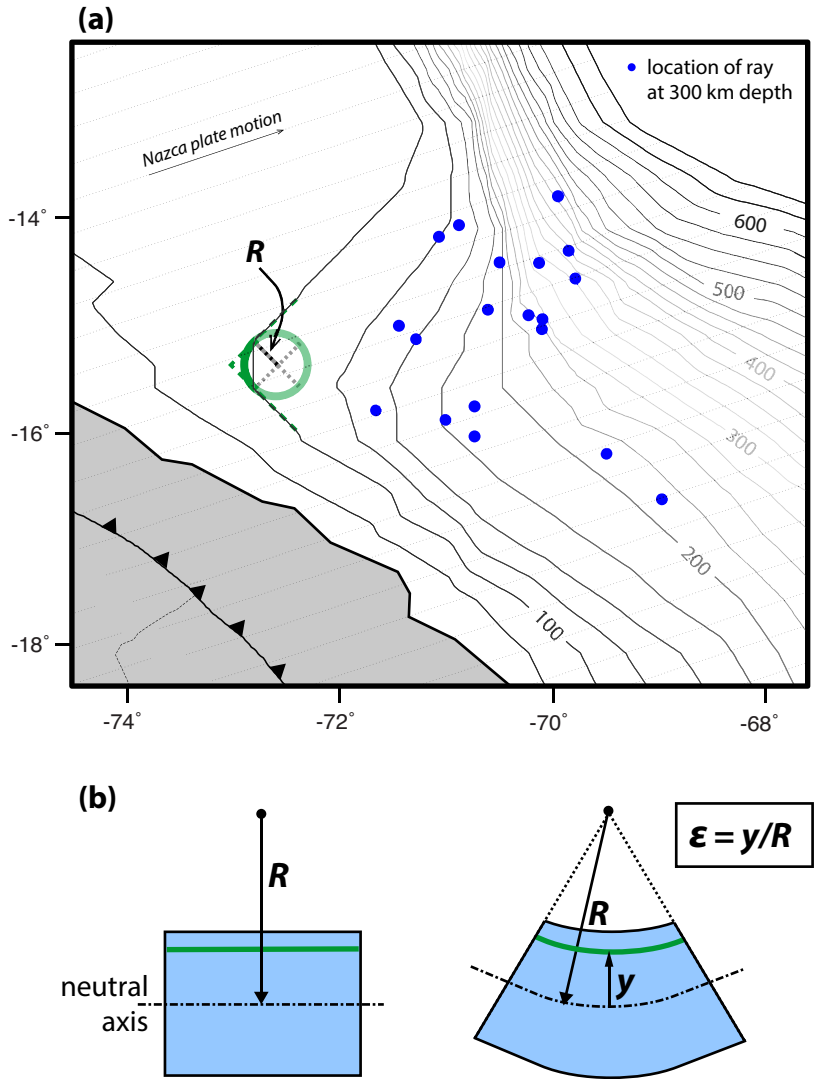

Figure S8. Illustration of the steps taken to estimate the bending strain. (a) First we take contours of the slab mid-point (zoomed in area of Figure 1), and measure the radius of curvature (R) for the tightest contour bend. This will provide an upper limit for the strain approximation. For the case shown (green circle) R is 33km. (b) We then estimate the lateral bending strain associated with the above contour bend. This follows the approximation from Turcotte and Schubert (pg 115)[19]. Strain will be zero along the neutral axis and increases with distance (y) away from the neutral axis. To estimate the maximum strain we equate y with the half plate thickness (i.e. at the slab edge). We therefore estimate the maximum strain from bending as 1-1.4 depending on the slab thickness 70-90 km.

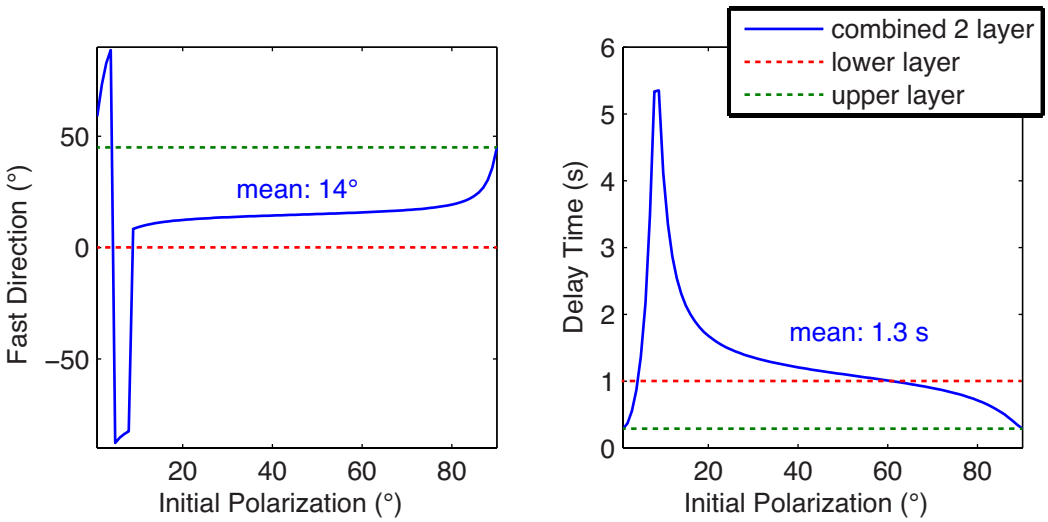

Figure S9. Predicted apparent splitting parameters assuming a two-layer anisotropic scenario in which a lower layer in the slab (ϕ: 0°, δt: 1.0s), is overlain by a weaker layer of anisotropy in the over-riding plate (ϕ: 45°, δt: 0.29s). A difference of 45° in the fast direction between the two layers is chosen to demonstrate the maximum possible impact. The effect of adding the additional upper layer of anisotropy is negligible on the slab splitting signal across most initial polarizations, as the difference between the average apparent splitting parameters and the true splitting parameters in the lower slab layer are only 14° for ϕ and 0.3 s for δt, which are smaller than the standard observational errors.

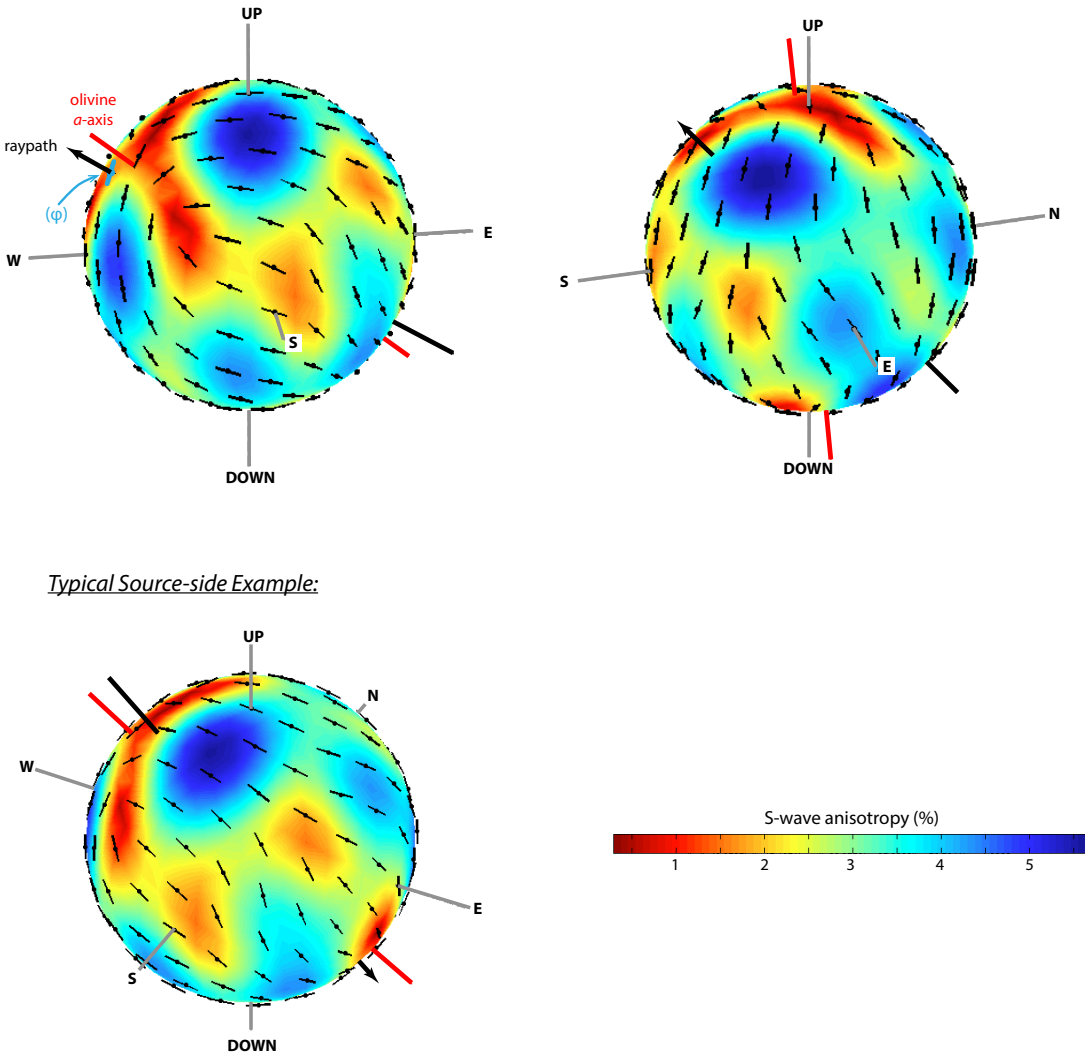

Figure S10. Illustrative examples of our modeling process showing typical local *S* and source-side raypath geometries. Multi-colored spheres are a visual representation of the 3D elastic tensor and predicted shear wave splitting behavior for A-type olivine [10], plotted using the MS_sphere function in MSAT [13]. The elastic tensors have been rotated into the predicted orientation of fossil fabric for the subducted slab, i.e. with the fast olivine *a*-axis approximately aligned with the slab down-dip direction. Black bars on the spheres represent the predicted fast-polarization acquired by a shear wave with a raypath piercing the sphere at that location. It is interesting to note that the raypaths are often aligned close to the olivine *a*-axis (i.e. the fast axis) as the rays are

mostly travelling along the length of the slab almost parallel to the slab dip. Such fossil fabric and ray geometries would therefore predict only a small degree of anisotropy (<2.5%; red-yellow colors shown), which is difficult to reconcile with large recorded delay times (Figure S6).

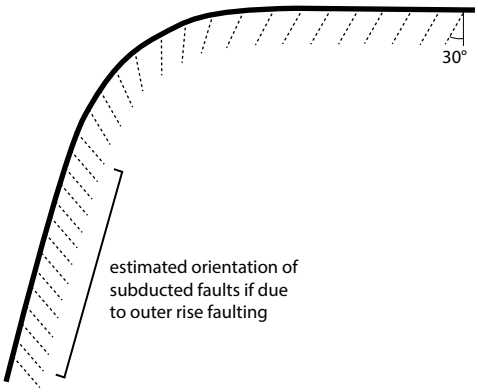

Figure S11. Cartoon sketch of the predicted orientation of faults in the upper part of the slab if they were due to bending and unbending at the outer rise[18]. The orientation of faulting predicted by the splitting observations in Figure S7b does not correspond to the faulting pattern shown here.

Depth (km)	Vp (km/s)	Vs (km/s)
0	5.8	3.35
5	5.8	3.35
5	6.2	3.53
moho	6.2	3.53
moho	8.04	4.48
77.5	8.04	4.48

Table S1. Velocity model for the Andean crust and upper mantle beneath PULSE and PeruSE stations used to calculate local *S* raypaths. Velocities for the rest of the mantle are derived from the iasp91 model [1]. The crustal velocity here is decreased compared to iasp91 to account for the dominantly felsic Andean crust. The Moho depth varies considerably beneath the stations from 22 to 72 km so we adjust the model for Moho depth at each station based on constraints from receiver functions [20]. This is the same background velocity model as was used for constructing the tomography.

Movie S1. Comparison of slab geometry and raypaths on which splitting measurements were made. The slab isosurface shown represents coherent fast anomalies (>3%) in the tomographic model [2]. Raypaths were calculated using the TauP toolkit [21] and based on the iasp91 velocity model [1], with a correction for the thicker Andean crust beneath PULSE and PeruSE stations. We chose the same crustal corrected velocity model as used in the tomographic inversion, the details of which are given in Table S1. (a) Raypaths are color-coded yellow for local *S* measurements and turquoise for source-side measurements. (b) Blue raypaths are those which are inferred to be mostly sensitive to slab material; red raypaths are not.

References

1. Kennett, B. L. N. & Engdahl, E. R. Traveltimes for global earthquake location and phase identification. *Geophys. J. Int.* **105,** 429–465 (1991).

2. Scire, A. *et al.* Imaging the transition from flat to normal subduction: Variations in the structure of the Nazca slab and upper mantle under southern Peru and northwestern Bolivia. *Geophys. J. Int.* (In Revision)

3. Faccenda, M. Water in the slab: A trilogy. *Tectonophysics* **614,** 1–30 (2014).

4. Foley, B. J. & Long, M. D. Upper and mid-mantle anisotropy beneath the Tonga slab. *Geophys. Res. Lett.* **38,** (2011).

5. Mohiuddin, A., Long, M. D. & Lynner, C. Mid-mantle seismic anisotropy beneath Southwestern Pacific subduction systems and implications for mid-mantle deformation. *Phys. Earth Planet. Inter.* **245,** 1–14 (2015).

6. Lynner, C. & Long, M. D. Heterogeneous seismic anisotropy in the transition zone and uppermost lower mantle: evidence from South America, Izu-Bonin and Japan. *Geophys. J. Int.* **201,** 1545–1552 (2015).

7. Nowacki, A., Kendall, J.-M., Wookey, J. & Pemberton, A. Mid-mantle anisotropy in subduction zones and deep water transport. *Geochemistry, Geophys. Geosystems* **16,** 764–784 (2015).

8. Eakin, C. M. & Long, M. D. Complex anisotropy beneath the Peruvian flat slab from frequency-dependent, multiple-phase shear wave splitting analysis. *J. Geophys. Res. Solid Earth* **118,** 4794–4813 (2013).

9. Eakin, C. M. *et al.* Response of the mantle to flat slab evolution: Insights from local S splitting beneath Peru. *Geophys. Res. Lett.* **41,** 3438–3446 (2014).

10. Karato, S. *Deformation of earth materials. An Introduction to the Rheology of Solid Earth*. 462 (Cambridge University Press, 2008).

11. Peselnick, L. & Nicolas, A. Seismic anisotropy in an ophiolite peridotite: Application to oceanic upper mantle. *J. Geophys. Res.* **83,** 1227 (1978).

12. Bunge, H. J. in *Preferred Orientation in Deformed Metal and Rocks: An Introduction to Modern Texture Analysis* (ed. Wenk, H. R.) 73–108 (Academic Press Inc, 1985). doi:10.1016/B978-0-12-744020-0.50009-2

13. Walker, A. M. & Wookey, J. MSAT—A new toolkit for the analysis of elastic and seismic anisotropy. *Comput. Geosci.* **49,** 81–90 (2012).

14. Gripp, A. E. & Gordon, R. G. Young tracks of hotspots and current plate velocities. *Geophys. J. Int.* **150,** 321–361 (2002).

15. Sinogeikin, S. V., Katsura, T. & Bass, J. D. Sound velocities and elastic properties of Fe-bearing wadsleyite and ringwoodite. *J. Geophys. Res.* **103,** 20819 (1998).

16. Sawamoto, H., Weidner, D. J., Sasaki, S. & Kumazawa, M. Single-Crystal Elastic Properties of the Modified Spinel (Beta) Phase of Magnesium Orthosilicate. *Science* **224,** 749–751 (1984).

17. Zha, C. *et al.* Single-crystal elasticity of β-Mg2SiO4 to the pressure of the 410 km seismic discontinuity in the Earth's mantle. *Earth Planet. Sci. Lett.* **147,** E9–E15 (1997).

18. Faccenda, M., Burlini, L., Gerya, T. V. & Mainprice, D. Fault-induced seismic anisotropy by hydration in subducting oceanic plates. *Nature* **455,** 1097–1100 (2008).

19. Turcotte, D. L. & Schubert, G. *Geodynamics*. (Cambridge University Press, 2002).

20. Bishop, B. *et al.* Receiver Function Study of the Peruvian Flat-Slab Region: Initial Results from PULSE. in *AGU Fall Meeting 2013* (2013).

21. Crotwell, H. P., Owens, T. J. & Ritsema, J. The TauP Toolkit: Flexible Seismic Travel-time and Ray-path Utilities. *Seismol. Res. Lett.* **70,** 154–160 (1999).